Rev. Roum. Sci. Techn.– Électrotechn. et Énerg.
Vol. **71**, *1*, pp. 45–52, Bucarest, 2026

A HYBRID INTELLIGENT CONTROL FRAMEWORK WITH REAL-TIME VALIDATION FOR INDUCTION MOTOR DRIVES

NGOC THUY PHAM[1]

Keywords: Backstepping; Radial basis function neural networks; Higher-order non-singular terminal sliding-mode control; Harris hawks' optimization; Chaotic Lévy flights.

This paper proposes a hybrid speed–current control framework for high-performance induction motor drives under field-oriented control. The outer speed loop combines Backstepping, Radial Basis Function neural approximation, and high-order sliding mode compensation, where Backstepping provides a Lyapunov-based nonlinear structure, the RBF network estimates lumped uncertainties online, and the HOSM term ensures finite-time disturbance rejection and fast convergence. An enhanced Harris Hawks Optimization with chaotic Lévy flights is employed to optimally tune the controller parameters. In the inner loop, a Higher-Order Non-Singular Terminal Sliding Mode controller regulates stator currents, guaranteeing finite-time tracking, reduced chattering, and robustness against parameter variations and inverter nonlinearities. Lyapunov analysis confirms uniform ultimate boundedness of the speed loop and finite-time convergence of the current loop. The effectiveness of the proposed strategy is verified through MATLAB/Simulink simulations and real-time implementation on the OPAL-RT OP5707XG platform, demonstrating superior dynamic performance and disturbance rejection compared with PI- and conventional sliding-mode-based schemes.

1. INTRODUCTION

Induction motors (IM) are widely used in industrial automation and electric vehicles due to their robustness, low cost, and high efficiency [1,2]. However, precise speed control remains challenging because of nonlinear coupled dynamics, load disturbances, and parameter variations, especially rotor resistance drift. Conventional FOC with PI controller is simple but lacks robustness under such uncertainties, often resulting in degraded transient response and limited disturbance rejection [3].

To improve performance, numerous nonlinear and intelligent control methods have been reported, including backstepping (BS), sliding mode control (SMC), high-order sliding modes (HOSM), neural and fuzzy approximation [4–19]. BS offers a Lyapunov-based design framework but is sensitive to modeling uncertainties [4–7]. RBF neural networks can approximate unmodeled dynamics, yet their compensation alone is insufficient under fast disturbances [8–12]. SM techniques provide strong robustness and finite-time convergence, but conventional SM may introduce chattering and degrade current-loop performance [13–16]. As a result, single-technique controllers often exhibit trade-offs among robustness, convergence speed, and torque smoothness. Hybrid Backstepping-based control schemes have been explored to overcome these limitations by integrating nonlinear mechanisms, including heuristic fuzzy gain tuning for improved transients but asymptotic convergence [17], and adaptive higher-order sliding-mode current control with gain-driven speed loops [18]. However, most approaches lack uncertainty estimation and do not ensure finite-time convergence.

To address these limitations, hybrid control structures that combine additional nonlinear techniques have attracted increasing attention in induction motor drive systems [19–31]. Following this approach, this paper proposes a hybrid BS–RBF–HONTSM speed control scheme integrated with an HONTSM current controller. Unlike the hybrid control schemes reported in [17] and [18], the proposed strategy is developed at the system-architecture level, rather than focusing on individual control algorithms. The RBF network and HONTSM are structurally embedded within the BS framework to shape the speed-loop dynamics, enabling fast transient response, reduced tracking error, and effective disturbance rejection. Moreover, the use of HONTSM in both the speed and current loops ensures coordinated finite-time dynamics and enhanced robustness. This development demonstrates a clear evolutionary progression from PI control [17] to NAHOSM with adaptive gain mechanisms [18] and further to HONTSM with non-singular finite-time convergence characteristics. In the speed control loop, the RBF network and HONTSM are directly integrated into the BS control framework, rather than serving as auxiliary BS tuning modules as in [17].

The performance of the proposed hybrid controller depends on several design parameters. Although various optimization methods have been reported in the literature, they often suffer from sensitivity to initial conditions, slow convergence, and entrapment in local optima [32–35]. These limitations motivate the adoption of an enhanced Harris Hawks Optimization with chaotic Lévy flights (EHHO-CLF) for offline parameter tuning. By improving exploration capability and alleviating premature convergence, EHHO-CLF ensures a well-balanced and robust controller configuration.

The proposed strategy is validated through MATLAB/Simulink simulations and real-time implementation on the OPAL-RT OP5707XG platform. Results confirm superior dynamic performance, strong disturbance rejection, and robustness against harmonic disturbances and rotor-resistance variations compared with conventional methods. The main contributions of this work include the proposed hybrid BS–RBF–HOSM structure, the HONTSM current regulator, EHHO-CLF-based parameter optimization, rigorous stability analysis, and comprehensive real-time validation.

The paper is organized as follows. Section 2 presents the induction motor model under FOC, Section 3 details the control design, Section 4 discusses simulation and real-time results, and Section 5 concludes the paper.

2. MATHEMATICAL DESCRIPTION OF IMDS

The mathematical model of the IM drive is formulated in the synchronously rotating reference frame to enable flux–

---

[1] Department of Electrical Technology, Industrial University of Ho Chi Minh City, Viet Nam. E-mail: phamthuyngoc@iuh.edu.vn

DOI: 10.59277/RRST-EE.2026.1.8

torque decoupling for FOC design [3]. The corresponding state-space model is given as follows:

$$\dot{x}(t)=\mathrm{A}x(t)+Bu(t) \tag{1}$$

where: x, A, B and u can be defined as:

$$A=\begin{bmatrix} a_{11} & 0 & a_{13} & a_{14} & a_{15} \\ 0 & a_{11} & -a_{14} & a_{13} & a_{25} \\ \dfrac{L_m}{\tau_r} & 0 & \dfrac{-1}{\tau_r} & \omega_r & \psi_{r\beta} \\ 0 & \dfrac{L_m}{\tau_r} & -\omega_r & \dfrac{-1}{\tau_r} & -\psi_{r\alpha} \\ -b\psi_{r\beta} & b\psi_{r\alpha} & bi_{s\beta} & -bi_{s\alpha} & \left(\dfrac{-B}{J}\right) \end{bmatrix};B=\begin{bmatrix} \dfrac{1}{\sigma L_s} & 0 & 0 \\ 0 & \dfrac{1}{\sigma L_s} & 0 \\ 0 & 0 & 0 \\ 0 & 0 & 0 \\ 0 & 0 & \dfrac{-1}{J} \end{bmatrix}$$

$$x(t)=\begin{bmatrix} i_{s\alpha} & i_{s\beta} & \psi_{r\alpha} & \psi_{r\beta} & \omega_r \end{bmatrix}^{\mathrm{T}};u(t)=\begin{bmatrix} u_{s\alpha} & u_{s\beta} & T_L \end{bmatrix}^{\mathrm{T}};$$

with $i_{s\alpha,\beta}$; $u_{s\alpha,\beta}$; $\varphi_{s\alpha,\beta}$ are components of the stator's current, stator's voltage and rotor's flux in the α-β reference frame. T_L is the load torque.

$$\tau_r=L_r/R_r;\ \sigma=1-\frac{L_m^2}{L_rL_s};\ \gamma=\frac{L_m}{L_r};\ k=\frac{3pL_m}{2L_r};\ b=\frac{k}{J};$$

$$a_{11}=-\frac{1}{\sigma L_s}\left(R_s+\frac{L_m^2}{L_r\tau_r}\right);\ a_{13}=\frac{\gamma}{\sigma L_s\tau_r};a_{14}=-\frac{\gamma}{\sigma L_s}\omega_r;$$
$$a_{15}=-\tfrac{\gamma}{\sigma L_s}\psi_{r\beta};\ a_{25}=\tfrac{\gamma}{\sigma L_s}\psi_{r\alpha} \tag{2}$$

L_s,L_r,L_m: stator, rotor, and mutual inductance ; R_s, R_r,: stator, rotor resistances; J: the inertia of motor; σ: total linkage coefficient; p: number of pole pairs; τ_r: rotor time constant; ω_r: rotor speed. Electromagnetic torque and the mechanical dynamics follow:

$$T_e=\tfrac{3}{2}p\tfrac{L_m}{L_r}\psi_{rd}i_{sq}, \tag{3}$$

$$J\frac{\mathrm{d}\omega_r}{\mathrm{d}t}=T_e-T_L-B\omega_r. \tag{4}$$

3. THE CONTROL DESIGN

3.1 BS–RBF–HONTSM SPEED-LOOP STRUCTURE

This section presents a BS-based speed controller enhanced with an RBF network and HONTSM to improve the control performance. The tracking errors are defined:

$$\begin{aligned} \varepsilon_\omega(t)&=(\omega_r^*-\omega_r)+k_\omega\int_0^t(\omega_r^*-\omega_r)\mathrm{d}t \\ \varepsilon_\psi(t)&=\left(\psi_{rd}^*-\widehat{\psi}_{rd}\right)+k_\psi\int_0^t\left(\psi_{rd}^*-\widehat{\psi}_{rd}\right)\mathrm{d}t \end{aligned} \tag{5}$$

The error dynamical equations:

$$\dot{\varepsilon}_\omega(t)=\dot{\omega}_r^*-\frac{3p}{2}\frac{\delta\sigma L_s}{J}\widehat{\psi}_{rd}i_{sq}+\frac{\hat{T}_l}{J}+B\omega_r+k_\omega(\omega_r^*-\omega_r)$$
$$\dot{\varepsilon}_\psi(t)=\dot{\psi}_{rd}^*+\tfrac{L_m}{\tau_r}i_{sd}+\tfrac{1}{\tau_r}\widehat{\psi}_{rd}+k_\psi\left(\psi_{rd}^*-\widehat{\psi}_{rd}\right) \tag{6}$$

where: k_ω, k_ψ are positive coefficients. Lyapunov function:

$$V_{(\omega,\psi)}(t)=\frac{1}{2}\left[\varepsilon_\omega^2(t)+\varepsilon_\psi^2(t)\right] \tag{7}$$

Differentiating V:

$$\frac{\mathrm{d}V_{(\omega,\psi)}}{\mathrm{d}t}=\varepsilon_\omega(t)\frac{\mathrm{d}\varepsilon_\omega(t)}{\mathrm{d}t}+\varepsilon_\psi(t)\frac{\mathrm{d}\varepsilon_\psi(t)}{\mathrm{d}t} \tag{8}$$

By substituting (6) into (8), we obtain:

$$+\varepsilon_\psi(t)\left\{\frac{\mathrm{d}\psi_{rd}^*}{\mathrm{d}t}+\frac{L_m}{\tau_r}i_{sd}^*+\frac{1}{\tau_r}\widehat{\psi}_{rd}+k_\psi\left(\psi_{rd}^*-\widehat{\psi}_{rd}\right)\right\} \tag{9}$$

To V'<0, the stabilizing virtual controls are chosen:

$$\begin{cases} i_{sq}^*=\frac{1}{b\widehat{\psi}_{rd}}\left\{k_\gamma\varepsilon_\omega(t)+\frac{\mathrm{d}\omega_r^*}{\mathrm{d}t}+B\omega_r+k_\omega(\omega_r^*-\omega_r)\right. \\ \qquad\left.+\frac{\hat{T}_l}{J}+\beta\left[u_{\omega\_RBF}(t)+u_{\omega\_HONTSMC}(t)\right]\right\} \\ i_{sd}^*=\frac{\tau_r}{L_m}\left\{k_\zeta\varepsilon_\psi(t)+\frac{\mathrm{d}\psi_{rd}^*}{\mathrm{d}t}+k_\psi\left(\psi_{rd}^*-\widehat{\psi}_{rd}\right)\right. \\ \qquad\left.+\frac{1}{\tau_r}\widehat{\psi}_{rd}+\lambda\left[u_{\psi\_RBF}(t)+u_{\psi\_HONTSMC}(t)\right]\right\} \end{cases} \tag{10}$$

T_L is the load torque, identified as in [25]. To determine $u_{i\text{-}RBF(t)}$, we have the following tracking errors defined as (5). Each neuron output is defined as follows:

$$\phi_j(x)=\exp\left(-\frac{\left\|x_i-c_j\right\|^2}{2\sigma^2}\right);x_i=\begin{bmatrix}\varepsilon_i(t)\\ \dot{\varepsilon}_i(t)\end{bmatrix};\ i=\omega{:}\psi \tag{11}$$

where $C_j=[C_{j\varepsilon},C_{j\dot{\varepsilon}}]^{\mathrm{T}}$ are pre-defined centers, and σ is the RBF width. The adaptive gains are obtained as:

$$\begin{aligned} K_{p\_i}(t)&=K_{p\_Op}+W_{p\_i}^{\mathrm{T}}\phi_i(x) \\ K_{i\_i}(t)&=K_{i\_op}+W_{i\_i}^{\mathrm{T}}\phi_i(x) \end{aligned} \tag{12}$$

with k_{pOp} *and* k_{i_Op} are positive coefficients and pre-optimized offline by EHHO-CLF. Weights are updated using gradient descent:

$$\dot{W}_{p\_i}=-\eta_{p\_i}\frac{\phi_i(x)\varepsilon_i(t)}{\left\|\phi_i(x)\right\|^2+\chi};\ \dot{W}_{i\_i}=-\eta_{i\_i}\frac{\phi_i(x)\varepsilon_i(t)}{\left\|\phi_i(x)\right\|^2+\chi} \tag{13}$$

where $n_{p\text{-}I}$ and $n_{i\text{-}i}$ are learning rates, and x=1e^{-5} avoids division by zero. Weight vectors are constrained in [-10^3 10^3] to prevent saturation. The $u_{i\text{-}RBF(t)}$ control signal is:

$$u_{i\_RBF}(t)=K_{pi}(t)\varepsilon_i(t)+K_{ii}(t)\int_0^t\varepsilon_i(\tau)\,\mathrm{d}\tau \tag{14}$$

A HONTSM in eq.(11) is adopted to ensure finite-time convergence, chattering reduction, and robust speed regulation. The sliding surface is defined as follows:

$$s_i(t)=\varepsilon_i(t)+\alpha_i|\varepsilon_i|^{p/q}\mathrm{sat}\left(\frac{\varepsilon_i(t)}{\zeta}\right) \tag{15}$$

with $\alpha_i>0$; $\zeta>0$; $0<p/q<1$ and they are pre-optimized offline by EHHO-CLF. The sliding surface is given by:

$$\begin{aligned} \dot{s}_i(t)=\dot{\varepsilon}_i(t)&+\alpha_i\frac{p}{q}|\varepsilon_i|^{(p/q)-1}\mathrm{sat}\left(\frac{\varepsilon_i(t)}{\zeta}\right) \\ &+\alpha_i|\varepsilon_i|^{(p/q)}\frac{\mathrm{d}}{\mathrm{d}t}\left[\mathrm{sat}\left(\frac{\varepsilon_i(t)}{\zeta}\right)\right] \end{aligned} \tag{16}$$

From (16), a HONTSM control law is designed:

$$u_{i\_HONTSMC}(t)=\frac{f_{1\_i}(s)}{f_{2\_i}(s)} \tag{17}$$

$$f_{1\_i}(s)=\dddot{s}_i+\frac{\left[\left(\ddot{s}_i+\dot{s}_i+|s_i|^{3/4}sat(s_i)\right)\left(|\dot{s}_i|+|s_i|^{3/4}\right)^{(-1/3)}\right]}{\left[\dot{s}_i+(|\dot{s}_i|+|s_i|^{3/4})^{(2/3)}\right]^{1/2}}$$

$$f_{2\_i}(s)=|\dddot{s}_i|+\left[|\dot{s}_i|+\left(|\dot{s}_i|+|s_i|^{3/4}\right)^{(2/3)}\right]^{1/2} \tag{18}$$

The stability of the proposed control scheme is analyzed using Lyapunov theory, with the following Lyapunov function:

$$\frac{\mathrm{d}V_{(\omega,\psi)}}{\mathrm{d}t} = -\varepsilon_\omega\left[k_\gamma\varepsilon_\omega + \beta\left[u_{\omega\_RBF} + u_{\omega\_HONTSMC}\right]\right]$$

$$-\varepsilon_\psi\left[k_\zeta\varepsilon_\psi + \lambda\left[u_{\psi\_RBF} + u_{\psi\_HONTSMC}\right]\right] \qquad (19)$$

Equation (19) can be rewritten as follows:

$$\frac{\mathrm{d}V_{(\omega,\psi)}}{dt} = -k_\gamma[\varepsilon_\omega]^2 - \beta\varepsilon_\omega\left[u_{\omega\_RBF}(t) + u_{\omega\_HONTSMC}\right]$$

$$-k_\zeta\left[\varepsilon_\psi\right]^2 - \lambda\varepsilon_\psi(t)\left[u_{\psi\_RBF} + u_{\psi\_HONTSMC}\right] \qquad (20)$$

We notice that β; λ; k_γ; k_ξ and $f_{2_i}(s)$ are always positive definite regardless of the sign of $s_i(t)$. So the sign of $\frac{\mathrm{d}V_{(\omega,\psi)}(t)}{\mathrm{d}t}$ depends entirely on the sign of:

$$F = -\varepsilon_\omega\left[u_{\omega\_RBF} + f_{1\_\omega}\right] - \varepsilon_\psi\left[u_{\psi\_RBF} + f_{1\_\psi}\right]$$

If $e_i > 0$, $u_{i\_RBF} > 0$, and $s_i > 0$ then $u_{i\_RBF} + f_{1\text{-}i} > 0$; if $e_i < 0$, $u_{i\_RBF} < 0$, and $s_i < 0$ then $u_{i\_RBF} + f_{1\text{-}i} < 0$

Therefore: $F(t) < 0$ with $\forall e_i(t)$. From (20), it follows that:

$$\frac{\mathrm{d}V_{(\omega,\psi)}}{dt} = -k_\gamma[\varepsilon_\omega(t)]^2 - \beta\varepsilon_\omega\left[u_{\omega\_RBF} + u_{\omega\_HONTSMC}\right]$$

$$-k_\zeta\left[\varepsilon_\psi\right]^2 - \lambda\varepsilon_\psi\left[u_{\psi\_RBF} + u_{\psi\_HONTSMC}\right] < 0 \quad \forall\varepsilon_\mathrm{i} \qquad (21)$$

Thus, the system is always stable according to Lyapunov stability theory. In this section, The differences with respect to [17] and [18] are clearly demonstrated. The RBF and HONTSM are structurally integrated into the BS framework to shape closed-loop dynamics, enabling fast transients, reduced tracking errors, and effective disturbance rejection.

3.2 PARAMETER OPTIMIZATION USING EHHO-CLF

The parameter vector to be optimized is defined as follows:

$$x = \left[c_1, \dots, c_n, \sigma_1, \dots, \sigma_n, w_1, \dots, w_n, K_{p,op}, K_{i,op}, \alpha, \beta\right] \qquad (22)$$

The objective is to minimize a multi-objective cost function*:*

$$J = w_1 ISE_\omega + w_2 ISE_T + w_3 M_p + w_4 T_s + w_5 TR \qquad (23)$$

where ISE_ω and ISE_T are integral squared errors for speed and torque tracking, M_p is the overshoot, T_s is the settling time, and *TR* is the electromagnetic torque ripple. Use logistic map to generate chaotic sequences instead of rand() in HHO (initialize population and choose probability of falling into regime):

$$\begin{aligned} &z_{n+1} = \mu z_n(1 - z_n); \quad \mu = 4; \quad z_0 \in (0,1) \\ &x_{i,j} = lb_j + z_{(i.j)}.\left(ub_j - lb_j\right);\ E_o = 2z_k - 1 \end{aligned} \qquad (24)$$

Definition of Lévy (Mantegna) step:

$$LF = 0.01\frac{u\sigma}{|v|^{1/\delta}}; \quad u \sim N(0, i^2); \quad \text{with } \delta \approx 1.5$$

$$\sigma = \left(\frac{\Gamma(1+\delta)\sin(\pi\delta/2)}{\Gamma\left(\frac{1+\delta}{2}\right)\delta 2^{(\delta-1)/2}}\right)^{1/\delta} \qquad (25)$$

The EHHO-CLF–optimized parameters initialize the HONTSM and RBF network. During real-time operation, the RBF network adapts to residual dynamics and disturbances, while the offline-tuned parameters ensure robust performance over varying operating conditions. The flowchart of the proposed EHHO-CLF algorithm is illustrated in Fig. 1.

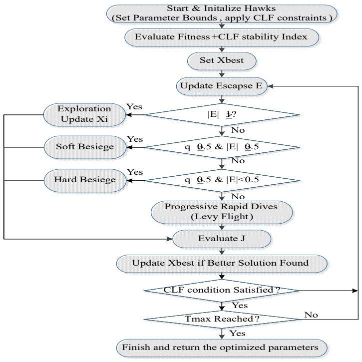

Fig. 1 – EHHO-CLF algorithm flowchart.

3.3 HONTSM-BASED CURRENT-LOOP STRUCTURE

The following tracking errors are defined:

$$\begin{cases} e_{isd} = i_{sd}^* - i_{sd} \\ e_{isq} = i_{sq}^* - i_{sq} \end{cases} \qquad (26)$$

To guarantee finite-time convergence and avoid singularities, the proposed sliding surface is defined as:

$$s_j(t) = e_j(t) + \alpha_j\left|e_j\right|^{\frac{p}{q}}\mathrm{sat}\left(\frac{e_j}{\zeta_j}\right); \quad j = \{isd; isq\}$$

$$\text{with: } \alpha_j > 0;\ \zeta_j > 0 \text{ and } 0 < \frac{p}{q} < 1 \qquad (27)$$

The derivative of the sliding surface is given by:

$$\begin{aligned} \dot{s}_j(t) = \dot{e}_j(t) + \alpha_j\frac{p}{q}\left|e_j\right|^{(p/q)-1}\mathrm{sat}\left(\frac{e_j}{\zeta_j}\right) \\ + \alpha_j\left|e_j\right|^{(p/q)}\frac{\mathrm{d}}{\mathrm{d}t}\left[\mathrm{sat}\left(\frac{e_j}{\zeta_j}\right)\right] \end{aligned} \qquad (28)$$

The Lyapunov function is selected as:

$$V = \frac{1}{2}s_j^2(t) = \frac{1}{2}\left[s_{isd}^2 + s_{isq}^2\right] \qquad (29)$$

Its derivative can obtain:

$$\frac{dV}{dt} = s_j(t)\dot{s}_j = s_{isd}\dot{s}_{isd} + s_{isq}\dot{s}_{isq} \qquad (30)$$

To satisfy $\frac{\mathrm{d}V(t)}{\mathrm{d}t} < 0$, then $s_j(t)\dot{s}_j(t) < 0$.

From eq. (28), a HONTSM control law is designed as follows:

$$\dot{s}(t) = -u_{HONTSMC}(t) = -\left[\beta_j u_j(t)\right] \qquad (31)$$

where: $$u_j(t) = \frac{f_{j1}(s_j)}{f_{j2}(s_j)} \qquad (32)$$

$$f_{j1} = \dddot{s}_j + \frac{\left[\left(\ddot{s}_j + \dot{s}_j + \left|s_j\right|^{3/4}sat(s_j)\right)\left(\left|\dot{s}_j\right| + \left|s_j\right|^{3/4}\right)^{(-1/3)}\right]}{\left[\dot{s}_j + \left(\left|\dot{s}_j\right| + \left|s_j\right|^{3/4}\right)^{(2/3)}\right]^{1/2}}$$

$$f_{j2} = \left|\dddot{s}_j\right| + \left[\left|\dot{s}_j\right| + \left(\left|\dot{s}_j\right| + \left|s_j\right|^{3/4}\right)^{(2/3)}\right]^{1/2}$$

Combining eq. (1), (28), (31), (32) and substituting the IM dynamics into the sliding condition the virtual control vector isq is designed as follows:

$$\begin{cases} u_{sd}^*(k) = \frac{L_s}{c}\left\{\frac{\mathrm{d}i_{sd}^*}{\mathrm{d}t} + ai_{sd} - L_s\omega_e i_{sq} - b\psi_{rd} + u_{isd}(t)\right\} \\ u_{sq}^*(k) = \frac{L_s}{c}\left\{\frac{\mathrm{d}i_{sq}^*}{\mathrm{d}t} + ai_{sq} - L_s\omega_e i_{sd} - b_r\omega_e\psi_{rd} + u_{isq}(t)\right\} \end{cases} \qquad (33)$$

Combining formulas (27), (30), (31) and (33) we get:

$$\frac{\mathrm{d}V(t)}{\mathrm{d}t} = s_j(t)\dot{s}_j(t) = -\beta_j s_j(t)u_j(t) \qquad (34)$$

where: β_j and $f_{j2}(s)$ are always positive definite regardless of the sign of s_j. So the sign of $\mathrm{d}V/\mathrm{d}t$ depends entirely on the sign of: $s_j f_{j1}$. From (28) we have:

If $e_j > 0$, $s_j > 0$, then $f_{j1} > 0$;

If $e_j < 0$, $s_j < 0$, then $f_j < 0$; hence $s_j f_{j1} > 0$ with $\forall\, e_j$.

From eq. (30) we have:

$$\frac{\mathrm{d}V(t)}{\mathrm{d}t} = s(t)\dot{s}(t) = -\beta_j s_j(t)u_j(t) < 0\ \forall e_j(t) \qquad (35)$$

Unlike [18], which applied NAHOSM only in the current loop, this work integrates HONTSM into both the speed and current loops, enabling coordinated finite-time dynamics.

4. RESULTS AND DISCUSSION

The BS-RBF–HONTSM control strategy was validated through MATLAB simulations and implemented on the OPAL-RT OP5707XG platform under strict real-time constraints using a IM with the rated parameters: 400 V, 50 Hz, 2 pole, 2880 rpm, R_s = 1.97 Ω, R_r = 1.96 Ω, L_s = 0.0154 H, L_r = 0.0154 H, L_m = 0.3585H, J = 0.00242 kg.m^2, B=0.0005. The proposed hybrid control framework is presented in Fig. 2.

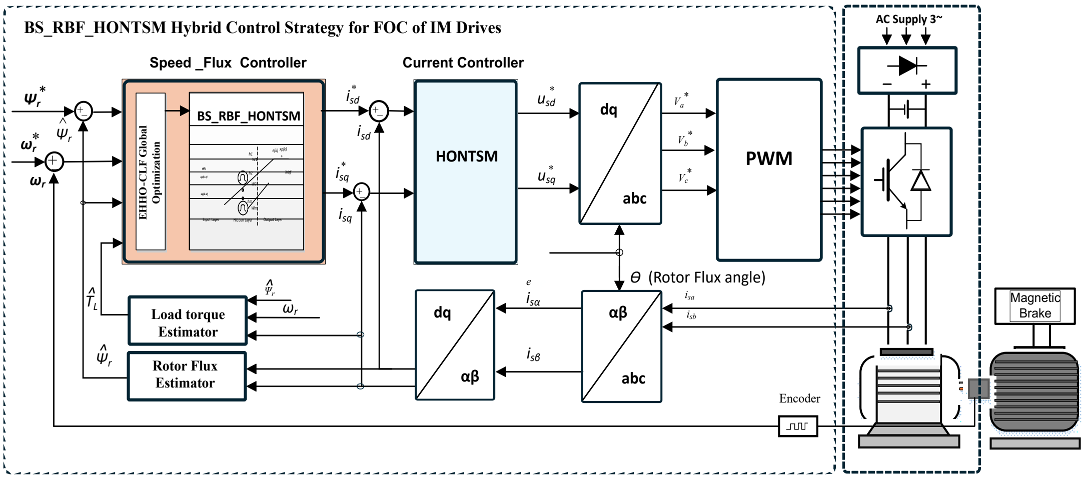

Fig. 2 – BS_RBF_HONTSM hybrid control framework for IM FOC drives.

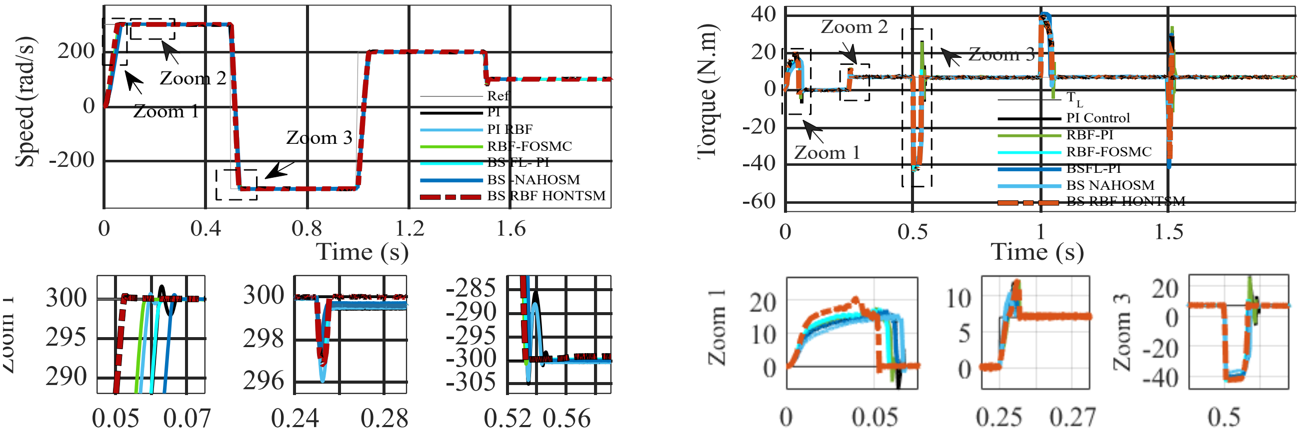

Fig. 3 – Performance of the controllers under the variable speed.

4. 1 SIMULATION TEST CONDITIONS

4.1.1 DYNAMIC PERFORMANCE

This section evaluates the IM drive performance under a speed reversal from +300 rad/s to −300 rad/s after acceleration to 100–200 rad/s, with a rated load of 7 Nm applied at t = 0.25 s. As shown in Fig. 3 and Table I, the BS–RBF–HONTSM strategy outperforms the PI, RBF-PI, RBF-FOSMC, BSFL-PI, and BS–NAHOSM schemes in terms of settling time, overshoot, ISE, and IAE. These results confirm the significantly improved dynamic response and disturbance rejection capability of the proposed controller. A more detailed comparison shows that, although the BSFL–PI controller in [17] offers fast response with low overshoot, it suffers from asymptotic convergence and limited robustness. The BS–NAHOSM scheme in [18] improves robustness but yields poor dynamics and large steady-state errors due to uncompensated load disturbances. In contrast, the proposed BS–RBF–HONTSM controller achieves the fastest settling time with the lowest ISE, IAE.

Table 1

Performance indices of different control strategies.

Control strategy	Setting Time	Overshoot	ISE	IAE
PI Control	0.0612	0.5504	0.0475	0.0949
RBF-PI	0.0581	0.2330	0.0410	0.0882
RBF-FOSMC	0.0568	0.0226	0.0068	0.0341
BSFL-PI	0.0630	0.0125	0.0089	0.0330
BS-NAHOSM	0.0648	0.1924	0.0018	0.1024
BS-RBF-HONTSM	0.0512	0.1768	0.0009	0.0097

4.1.2 ROBUSTNESS ANALYSIS AGAINST HARMONIC DISTURBANCES AND RANDOM

To evaluate robustness against periodic disturbances, harmonic torque components were injected into the drive system, following a procedure like [15]. The dominant 1st, 4th, and 12th harmonic orders were considered, corresponding to mechanical misalignment and cogging effects. Tests were conducted at 100 rpm and 600 rpm, where the disturbance torque is expressed as (36).

$$T_d(k) = T_{co}\cos(m\theta) + T_{si}\sin(m\theta) \qquad (36)$$

where *Tco, Tsi* are the *m-th* harmonic sine and cosine components. In this case, at 100 and 600 rpm speed, the harmonic frequencies appear 1.66, 6.66, 20 Hz and at 10, 40 and 120 Hz, respectively, (the first, fourth, and 12th harmonic orders). Fig. 4 show that PI controller exhibits significant performance degradation, with large speed and torque oscillations at both speeds due to its fixed gains. In contrast, BS–RBF–HONTSM controller effectively attenuates harmonic disturbances, maintaining smooth and accurate speed tracking across the operating range.

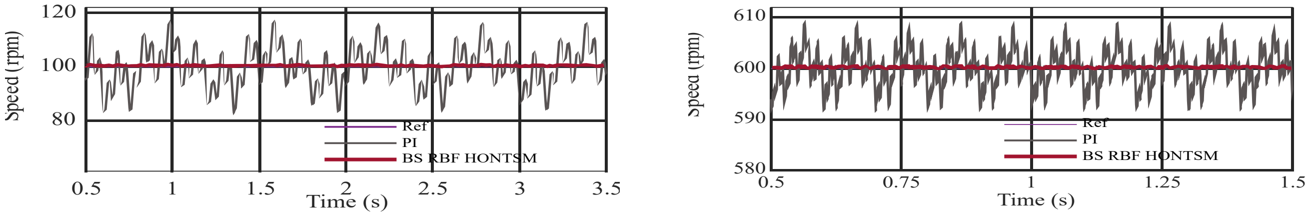

Fig. 4 The speed responses of PI and BS RBF HONTSM control under harmonic torque disturbance at 100 rpm and 600 rpm

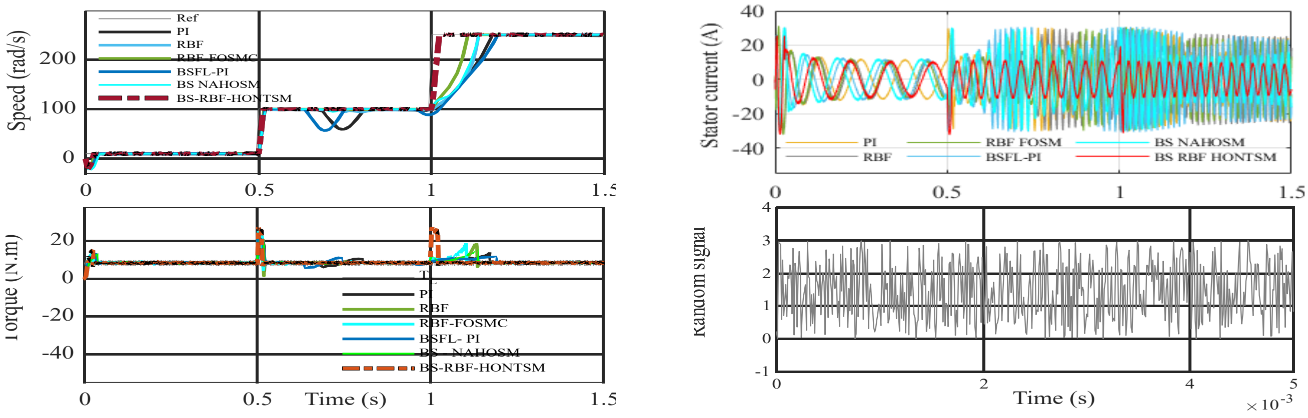

Fig. 5 – Controller performance under 7 N·m load and random disturbance.

To further assess robustness, the system was tested under constant load with random disturbances and variable-speed operation. As shown in Fig. 5, only the proposed controller effectively rejects these disturbances while maintaining stable trajectories, whereas the PI, RBF, and RBF-FOSMC, BSFL-PI and BS-NAHOSM controllers exhibit oscillations and degraded tracking performance.

A detailed comparison in Fig. 5 shows that the BSFL–PI controller in [17] suffers from degraded stability under random disturbances due to heuristic fuzzy tuning, lack of explicit disturbance compensation, and a fixed-parameter PI current loop. The BS–NAHOSM controller in [18] improves disturbance rejection via an adaptive HOSM current loop but still exhibits limited dynamic response. Overall, the BS–RBF–HONTSM strategy demonstrates superior disturbance rejection, improved transient response, and strong robustness under harmonic and stochastic disturbances.

4.1.3 ROBUSTNESS ANALYSIS AGAINST PARAMETRIC UNCERTAINTIES

To further assess robustness against parameter variations, the rotor resistance of the induction motor was intentionally doubled during operation. The motor ran at a constant speed of 95 rpm, and a load step from no-load to rated load was applied at $t = 0.2$s. Fig. 6 shows the speed, torque, and current responses for the conventional PI and the proposed controllers. When the rotor resistance increases, the PI controller exhibits significant performance degradation, including speed drop and pronounced oscillations, which become more severe at higher speeds. In contrast, the proposed controller maintains stable operation throughout the test, with smooth current responses and nearly zero steady-state speed error, demonstrating strong robustness against parameter uncertainties.

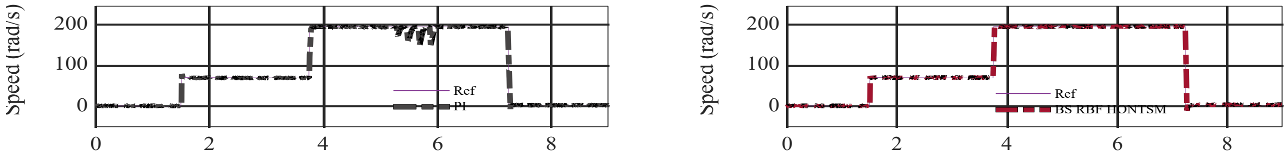

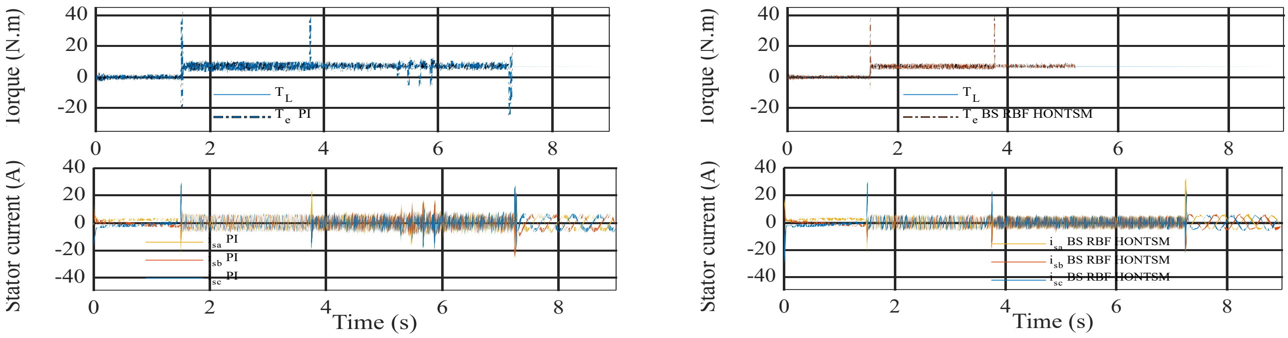

Fig. 6 – Robustness of PI and BS-RBF-HONTSM under the variable parameter motor ($R_r = 2R_{r,nom}$).

4.2 REAL-TIME IMPLEMENTATION

To evaluate the practicality and real-time feasibility of the proposed control scheme, the full controller–plant structure was implemented on the OPAL-RT OP5707XG platform under strict real-time constraints. The overall real-time execution framework of the proposed control strategy on the OPAL-RT OP5707XG platform is illustrated in Fig. 7, and the laboratory setup used for validating the proposed solution is shown in Fig. 8.

4.2.1 DYNAMIC PERFORMANCE

In this experiment, the reference speed was setup from 0 to 2860 rpm, reversed to −2860 rpm at t = 3 s, and varied again under rated load at t =1 s. The BS–RBF–HONTSM controller accurately tracks all transitions with fast settling, negligible overshoot, and low ripple.

The OP5707XG real-time results in Fig. 9 closely match the simulations in Fig. 3. The PI controller exhibits oscillations near zero speed, delayed torque response, and slower recovery due to computation delay and quantization effects. In contrast, the proposed controller maintains smooth torque and current responses with clean zero-speed crossing and no chattering, demonstrating superior performance during rapid acceleration, speed reversal, and zero-crossing operation.

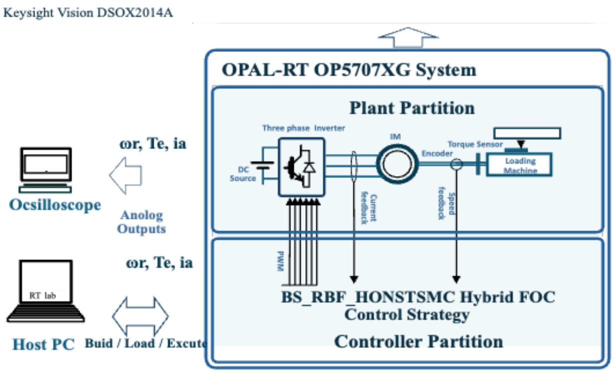

Fig. 7 – Overall real-time execution framework on the OPAL-RT-5707XG platform.

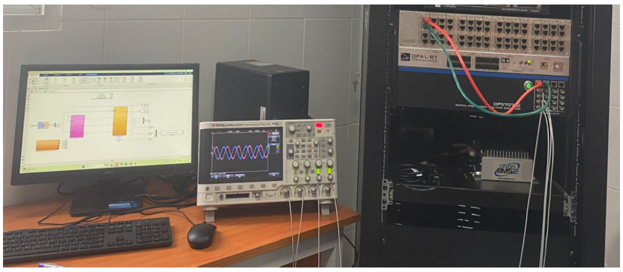

Fig. 8 – Laboratory setup for proposed solution.

4.2.2 ROBUSTNESS ANALYSIS AGAINST HARMONIC DISTURBANCES

To match the simulation setup, harmonic disturbances were injected into the real-time plant at 100 rpm and 600 rpm. As shown in Fig. 10 (a) and (b), the PI controller suffers from significant speed and torque oscillations under harmonic loading due to its fixed gains. In contrast, the proposed BS–RBF–HONTSM controller effectively suppresses harmonic effects, maintaining smooth torque, low speed ripple, and accurate tracking at both speeds. The close agreement between real-time and simulation results further confirms the robustness and reliability of the proposed controller under realistic harmonic disturbance conditions.

4.2.3 ROBUSTNESS ANALYSIS AGAINST PARAMETER VARIATION

To evaluate robustness against parameter variations, the rotor resistance was doubled in real-time $\left(R_r = 2R_{r,\text{nom}}\right)$to emulate severe thermal drift. Under this condition, the PI controller exhibits significant degradation, including strong speed oscillations, current spikes, torque distortion, and a tendency toward instability at higher speeds. In contrast, the proposed BS-RBF-HONTSM controller maintains smooth speed tracking, low current ripple, and well-damped torque dynamics, rapidly recovering after the parameter change. Although simulation in Fig. 6 and real-time results in Fig. 11 show similar trends, real-time execution reveals much stronger sensitivity of the PI controller to parameter mismatch. The proposed controller, however, demonstrates nearly identical behavior in both environments, confirming superior robustness to rotor resistance variation and real-time execution constraints.

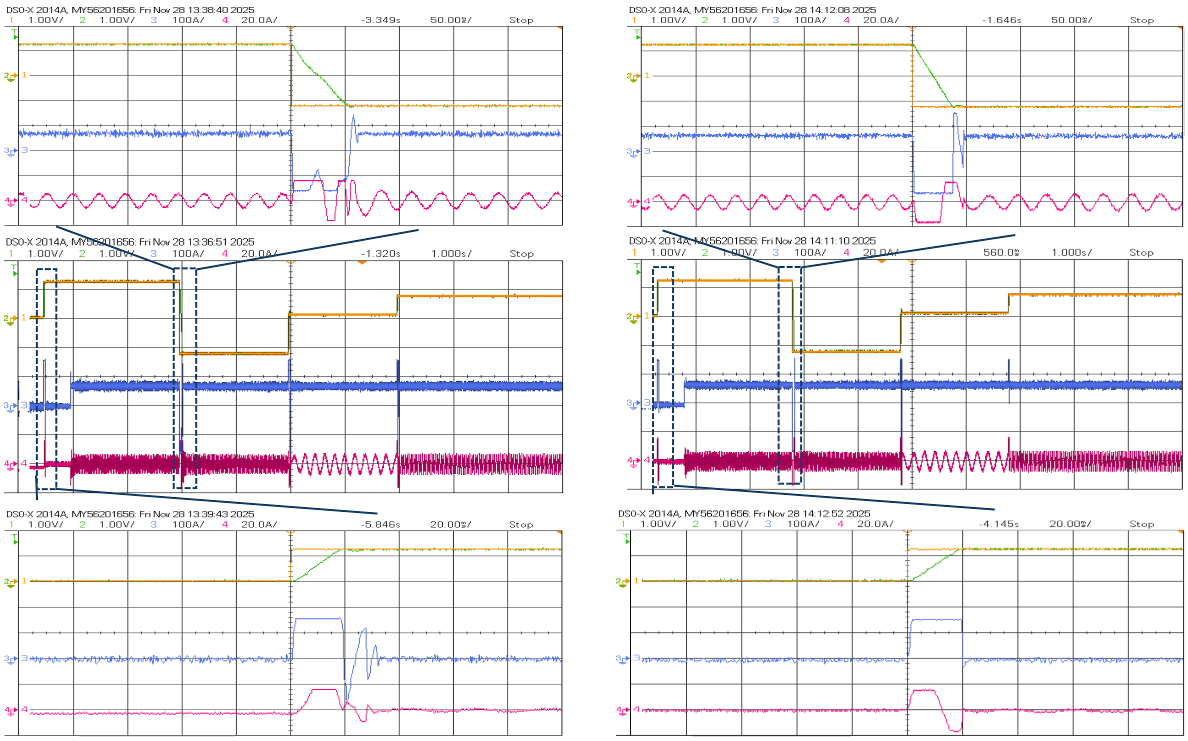

Fig. 9 – Real-time variable-speed responses for PI (left) and BS–RBF–HONTSM (right): speed, torque, and phase-a current.

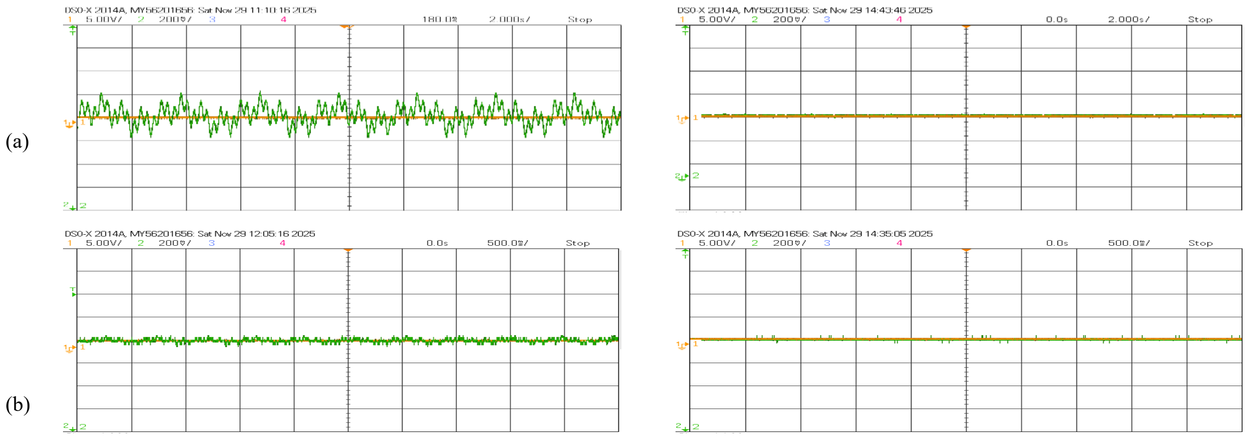

Fig. 10 – Real-time responses at (a) 100 rpm and (b) 600 rpm under harmonic torque disturbance comparing PI (left) and BS–RBF–HONTSM (right) controllers: speed response

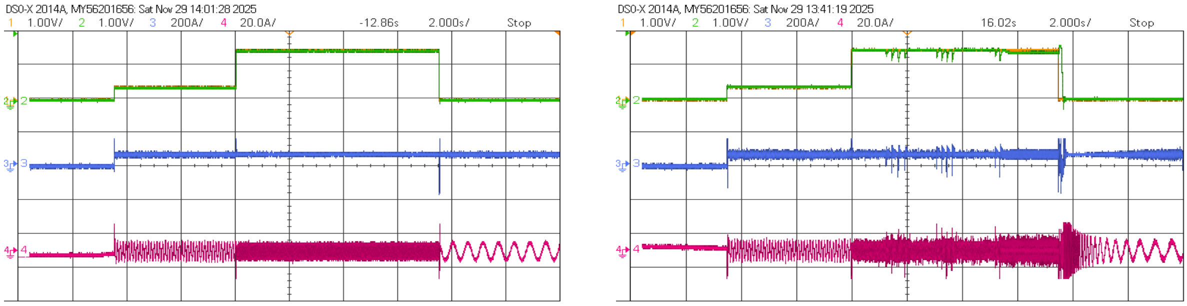

Fig. 11 – Real-time responses under doubled rotor resistance: comparison of PI (left) and BS–RBF–HONTSM (right) controllers showing speed, torque, and phase-a current.

5. CONCLUSION

This work presents a unified hybrid control strategy that integrates BS, RBF compensation, and HOSM techniques for high-performance IM drives. By combining Lyapunov-based nonlinear design with adaptive approximation and finite-time robust compensation, the proposed controller overcomes the limitations of conventional PI, pure neural, and classical SM schemes. Compared with previously reported in [17,18], the proposed framework represents a significant methodological advancement in control architecture, closed-loop dynamic performance, and system-level robustness. This results in faster transient response, superior disturbance rejection, and consistently improved performance under aggressive operating conditions.

The effectiveness of the proposed BS-RBF-HONTSM framework is validated through extensive MATLAB/Simulink simulations and real-time experiments on the OPAL-RT OP5707XG platform. The results demonstrate fast dynamic response, strong robustness against harmonic disturbances and parameter variations, and consistent performance under real-time execution constraints, including computation delay and quantization effects. Future work will focus on power-hardware-in-the-loop validation, integration of adaptive load-torque observers, and FPGA-based implementation for next-generation electric drive systems.

Received on 24 December 2025

REFERENCES

1. A.M.N. Lima, C.B. Jacobina, E.B. de Souza Filho, *Nonlinear parameter estimation of steady-state induction machine models*, IEEE Transactions on Industrial Electronics, **44**, *3*, pp. 390–397 (1997).
2. J. Pyrhönen, V. Hrabovcová, R.S. Semken, *Electrical machine drives control*, John Wiley & Sons Ltd (2016).
3. I.M. Mehedi, N. Saad, M.A. Magzoub, U.M. Al-Saggaf, A.H. Milyani, *Simulation analysis and experimental evaluation of improved field-oriented controlled induction motors incorporating intelligent controllers*, IEEE Access, **10**, pp. 18380–18394 (2022).
4. A. Benheniche, A. Berrezzek, *Integral backstepping control of induction machine*, European Journal of Electrical Engineering, **23**, *4*, pp. 345–351 (2021).
5. C. Melkia, M. Attia, R. Daouadi, K. Raïs, *Improved PMSM speed control using backstepping: stability and performance analysis*, Journal of European Systems and Automation, **58**, pp. 383–392 (2025).
6. N. Ali, W. Alam, M. Pervaiz, J. Iqbal, *Nonlinear adaptive backstepping control of permanent magnet synchronous motor*, Rev. Roum. Sci. Techn. – Électrotechn. et Énerg., **66**, pp. 9–14 (2021).
7. H. Djouadi, K. Ouari, Y. Belkhier, H. Lehouche, M. Bajaj, V. Blazek, *Improved robust model predictive control for PMSM using backstepping control and incorporating integral action with experimental validation*, Results in Engineering, **23**, 102416 (2024).
8. N. Pham, T. Le, *A novel FOC vector control structure using RBF tuning PI and SM for SPIM drives*, International Journal of Intelligent Engineering and Systems, **13**, pp. 429–440 (2020).
9. R.S. Kumar et al., *A combined HT and ANN based early broken bar fault diagnosis approach for IFOC fed induction motor drive*, Alexandria Engineering Journal, **66**, pp. 15–30 (2023).
10. C.M. Lee, C.F. Liang, J.C. Hung, *Adaptive control of a permanent magnet synchronous motor based on radial basis function neural networks*, IEEE Transactions on Energy Conversion, **38**, *2*, pp. 411–420 (2023).
11. Y. Xu, B. Huang, Y. Sun, *Adaptive RBF neural network-based control for uncertain nonlinear systems*, Automatica, **158**, 111234 (2023).
12. N. Farah et al., *A novel self-tuning fuzzy logic controller-based induction motor drive system: an experimental approach*, IEEE Access, **7**, pp. 68172–68184 (2019).
13. X. Li, J. Liu, Y. Yin, K. Zhao, *Improved super-twisting non-singular fast terminal sliding mode control of interior permanent magnet synchronous motor considering time-varying disturbance*, IEEE Access, **11**, pp. 17485–17496 (2023).
14. Z. Kang et al., *Adaptive generalized super-twisting sliding mode control for PMSM drives*, IEEE Transactions on Energy Conversion, **138**, pp. 639–649 (2023).
15. N. Abou-Qamar, C. Hatziadoniu, *Cancellation of harmonic torque disturbance in permanent magnet synchronous motor drives by using an adaptive feedforward controller*, IET Power Electronics, **11**, *14*, pp. 2215–2221 (2018).
16. B. Xu, L. Zhang, W. Ji, *Improved non-singular fast terminal sliding mode control with disturbance observer for PMSM drives*, IEEE Transactions on Transportation Electrification, **7**, *4*, pp. 2753–2762 (2021).
17. N.T. Pham, P.D. Nguyen, *A novel hybrid backstepping and fuzzy control for three phase induction motor drivers*, International Journal of Robotics and Control Systems, **5**, *1*, pp. 599 (2025).
18. N.T. Pham, *An improved BS_NAHOSM hybrid control strategy for FOC of dual star induction motor drives*, Periodica Polytechnica Electrical Engineering and Computer Science, **69**, *3*, pp. 226–235 (2025).
19. S. Ali, A. Prado, M. Pervaiz, *Hybrid backstepping–super twisting algorithm for robust speed control of a three-phase induction motor*, Electronics, **12**, 681 (2023).
20. T. Workineh, Y. Kassie, A. Abrham, *Evaluation of intelligent PPI controller for the performance enhancement of speed control of induction motor*, Scientific African, **22**, 101982 (2023).
21. G.K. Alitasb, *Integer PI, fractional PI, and fractional PI data trained ANFIS speed controllers for indirect field-oriented control of induction motor*, Heliyon, **10**, *18* (2024).
22. B. Aichi, K. Kendouci, *A novel switching control for induction motors using a robust hybrid controller that combines sliding mode with PI anti-windup*, Periodica Polytechnica Electrical Engineering and Computer Science, **64**, *4*, pp. 392–405 (2020).
23. R. Rouabhi, A. Herizi, S. Djeriou, A. Zemmit, *Hybrid type-1 and 2 fuzzy sliding mode control of the induction*, Rev. Roum. Sci. Techn. – Électrotechn. et Énerg., **69**, *2*, pp. 147–152 (2024).
24. N.T. Pham, K.H. Nguyen, *Novel nonlinear control structure for vector control of SPIM drive using BS PCH*, International Journal of Power Electronics and Drive Systems, **11**, *2*, pp. 1099–1108 (2020).
25. L.B. Somasundaram, *Sliding mode controlled closed loop QB-converter-TPIS fed PMSM drive with enhanced response*, Rev. Roum. Sci. Techn. – Électrotechn. et Énerg., **70**, *3*, pp. 331–336 (2025).
26. N.T. Pham, *Sensorless speed control of SPIM using BS_PCH novel control structure and NNSM_SC MRAS speed observer*, Journal of Intelligent & Fuzzy Systems, **39**, *3*, pp. 2657–2677 (2020).
27. H. Benderradji, S. Benaicha, Y. Laamari, *Combined first and second-order sliding mode control of induction motor*, Rev. Roum. Sci. Techn. – Électrotechn. et Énerg., **69**, *4*, pp. 389 (2024).
28. F.M. El-Sousy, M.M. Amin, O.A. Mohammed, *Robust adaptive neural network tracking control with optimized super-twisting sliding-mode technique for induction motor drive system*, IEEE Transactions on Industry Applications, **58**, *3*, pp. 4134–4157 (2022).
29. A. Rubaai, P. Young, *EKF-based PI-/PD-like fuzzy-neural-network controller for brushless drives*, IEEE Transactions on Industry Applications, **47**, *6*, pp. 2391–2401 (2011).
30. P. Ma, J. Yu, Q.-G. Wang, J. Liu, *Filter- and observer-based finite-time adaptive fuzzy control for induction motor systems considering stochastic disturbance and load variation*, IEEE Transactions on Power Electronics, **38**, *2*, pp. 1599–1609 (2023).
31. H. Rafia, H. Ouadi, F. Giri, E.B. Brahim, *Advanced hybrid control for induction motor combining ANN-PID speed controller with neural predictive current regulator based on particle swarm optimization*, Transactions of the Institute of Measurement and Control (2024).
32. R. Thangaraj, T.R. Chelliah, M. Pant, A. Abraham, C. Grosan, *Optimal gain tuning of PI speed controller in induction motor drives using particle swarm optimization*, Logic Journal of the IGPL, **19**, *2*, pp. 343–356 (2011).
33. M. Chebre, A. Meroufel, Y. Bendaha, *Speed control of induction motor using genetic algorithm-based PI controller*, Acta Polytechnica Hungarica, **8** (2011).
34. L. Hong, Y. Mo, D. Bao, R. Gong, *Chaos elite Harris Hawk optimization algorithm to solve chemical dynamic optimization problems*, IEEE Access, **10**, pp. 65833 (2022).
35. K. Abraham Mathew, D. Harish, *Speed regulation of PMSM drive in electric vehicle applications with sliding mode controller based on Harris Hawks optimization*, e-Prime: Advances in Electrical

Engineering, Electronics and Energy, **9**, 100643 (2024).